Levoglucosenone to 3D-printed green materials: synthesizing sustainable and tunable monomers for eco-friendly photo-curing

Amandine Flourat, Lorenzo Pezzana, Sabrina Belgacem, Abdouramane Dosso, Marco Sangermano, Sami Fadlallah, Florent Allais

Levoglucosenone to 3D-Printed Green Materials: Synthesizing Sustainable and Tunable Monomers for Eco-Friendly Photo-curing

Amandine L. Flourat,[a§] Lorenzo Pezzana,[b§] Sabrina Belgacem,[a] Abdouramane Dosso,[a] Marco Sangermano,[b] Sami Fadlallah*[a†] and Florent Allais*[a†]

Abstract: 3D-printing technologies for polymeric formulations are experiencing a huge development due to the complex and specific geometries that can be covered employing additive manufacturing. However, to ensure sustainable growth, it is essential to replace the currently used fossil-based resins with new bio-sourced alternatives. In this study, tunable bis-allylated compounds were efficiently synthesized from cellulose-derived levoglucosenone via a chemo-enzymatic pathway whom greenness has been assessed by E-factor and Eco-Scale. Subsequently, photocuring was employed as an eco-friendly process to polymerize these compounds with a trifunctional thiol using thiol-ene click chemistry. Real-time techniques such as FT-IR, photo-DSC, and photo-rheology were employed to extensively characterize the UV-process. The resulting thermosets were also subjected to a thorough analysis, covering their thermal-mechanical properties and degradation. Owing to the exceptional reactivity of this thiol-ene system, 3-D printed materials were achieved with remarkable precision.

Introduction

Over the past few decades, there has been a growing focus within the scientific community on reducing the use of fossil-based material and promoting sustainability.[1,2] Bio-based chemicals are increasingly seen as a key player in the transition from petroleum-based materials towards new green materials derived from bio-based feedstock. Among the primary sources for these chemicals, cellulose, lignocellulose and lignin are the main components that can be converted into a range of different chemicals for various applications.[3–6] One particularly promising candidate for creating more sustainable materials is cellulose-derived levoglucosenone (**LGO**), which has the added benefit of being produced through a carbon neutral process.[7] This chiral synthon - obtained through the flash catalytic pyrolysis of cellulose - exhibits various chemical functions allowing a wide range of transformations (*e.g.*, α,β-unsaturated ketone). [8] Recently, we have been concentrating on developing new types of functional monomers using **LGO**, taking advantage of its highly reactive functionalities and commercial availability (currently at 50 T/yr and soon increasing to 1000 T/yr). These new **LGO** polymer derivatives include polyacrylates,[9] polycyclic olefins,[10] polyesters,[11,12] and polycarbonates.[13] However, until now, the controlled formation of polymer networks derived from **LGO** monomers has not been reported.[14] Furthermore, combining bio-based polymers with eco-friendly polymerization technology represent a step further to limit cost production, energy consumption and time. UV-curing is particularly appealing due to its ability to minimize volatile organic compounds (VOCs) emissions, it also requires mild curing condition, and eliminates oxygen inhibition.[15]

Among the UV-curing-based technologies, thiol-ene click chemistry represents an attractive process which allows high conversion due to the click-characteristic (*i.e.*, a 1:1 reaction between thiol and ene functionalities) and the lack of oxygen inhibition.[16–18] This chemistry has been explored with several bio-based platforms in recent years, such as levoglucosan,[19] terpenes,[20,21] furans,[22,23] isosorbide derivatives.[24–26] However, to the best of our knowledge, no studies have been conducted on the UV-curing of levoglucosenone derivatives. Additive manufacturing (AM) technology represent an evolution of UV-curing, which allows to get complex and self-stain geometry, that is continuously growing due to the multiple applications from biomedical to aerospace.[27,28] Among the available technics, digital light processing (DLP) represents a well-established technology that allows to cure a liquid polymer resin using UV-irradiation.[29,30] One current challenge is the growth and expansion of possible bio-based resin that can be used in 3D printing.[31,32]

Vanillin-based acrylate material has been used in thiol-ene chemistry showing a promising platform for bio-based resins.[33,34] Linalool derivatives has been used in DLP showing good printability for complex prototypes and good

thermo-mechanical properties.[35] Also, other terpenes have been used, as limonene and myrcene,[36] demonstrating the possibility to shift towards green resins.

In this framework, the aim of this study is to develop a new set of bio-based tailored monomers suitable for thiol-ene UV-curing and to test the resulting resins in a DLP printing, thus increasing the possible applications. A new class of bis-allyl monomers has been synthesized from **LGO** through oxa-Michael addition, catalyst- and solvent-free Baeyer-Villiger oxidation[37,38] and enzymatic transesterification with several bio-sourced diesters. The eco-friendliness of this pathway was characterized through E-factor[39] and EcoScale[40] calculations. Furthermore, the monomers' chain length can be varied to fine-tune material properties, and the ester bonds can be susceptible to degradation at the end of the material's life.[19,41] To this end, the polythiol chosen in this study, trimethylolpropane tris(3-mercaptopropionate) (TMPMP), encompasses ester linkages in its backbone. The photo-crosslinking between bis-allylated monomers and TMPMP was investigated through different technics (*i.e.*, real-time FTIR, photo-DSC and photo-rheology) and proved very efficient. The new materials were characterized through DSC, DMTA, tensile-test and TGA prior successful assays of 3D-printing. The degradability of the bio-based resin was investigated by hydrolytic degradation to prove its potential for chemical recycling.

Results and Discussion

Synthesis of monomers

As mentioned earlier, LGO is a versatile starting material due to its multifunctionality, which enables numerous reactions.8 Various oxa-Michael addition on the β-position of the α,β- unsaturated ketone were reported with water,42 benzyl alcohol,43 ethanol44 or citronellol13,45. However, in all cases, a large excess of alcohol was necessary to not only achieve a maximum conversion of LGO into the desired product, but also limit its dimerization into LGO-Cyrene. With the aim to introduce a terminal alkene function, allyl alcohol was added into LGO (Scheme 1). To determine the optimal reaction conditions for oxa-Michael addition, initial experiments were conducted using acidic or basic conditions. Although acidic catalysis (HCl) led to slightly higher yield based on NMR (83% vs 77%), basic condition was chosen as it did not require any additional treatment at the end of the reaction. Specifically, triethylamine, used as an activator of the reaction, was readily evaporated during the concentration step, whereas hydrochloric acid needed to be neutralized with a base, resulting into salts that had to be removed through filtration after concentration.

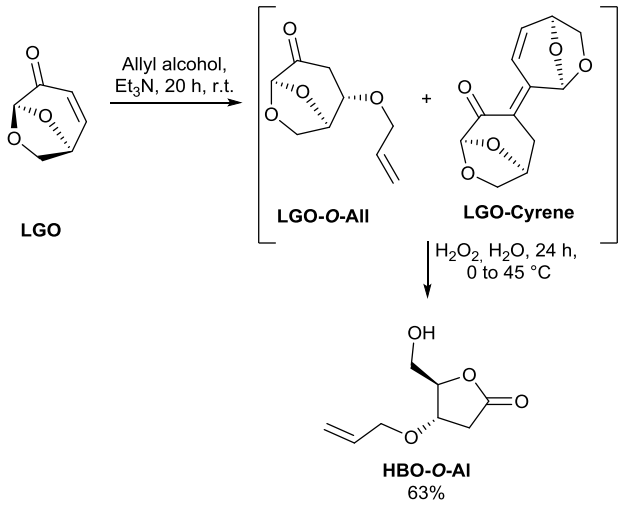

*Scheme 1. Synthesis of **HBO-O-All** from **LGO***

The impact of the excess of allyl alcohol was evaluated using 5 to 100 equiv. (Figure 1), and yields greater than 75% (determined by NMR) were achieved when more than 20 equivalents were used. However, the formation of the dimer LGO-Cyrene (>10% yield) was observed as a major byproduct. To limit the formation of this undesired compound, an even higher excess of allyl alcohol was

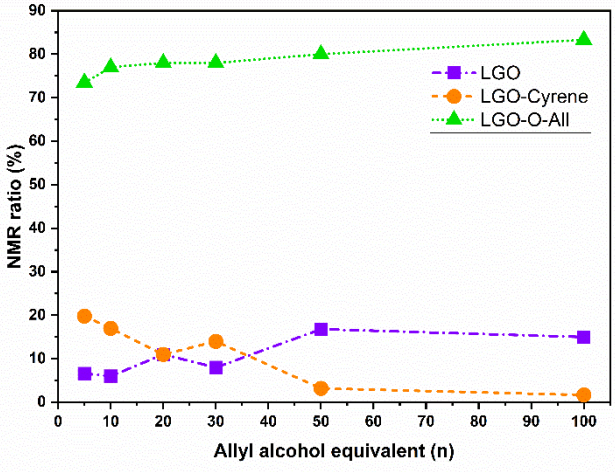

***Figure 1.** Evolution of the ratio between **LGO** (violet), **LGO-Cyrene** (orange) and desired **LGO-O-All** (green) in function of engaged equivalent of allyl alcohol*

required (50 equiv.). It is worth mentioning that more than 95% of unreacted allyl alcohol was recovered after distillation. To achieve full drying, a high vacuum with a pressure of 10-7 bar was applied. However, this resulted in a decrease in the yield of LGO-O-All and an increase in LGO, indicating that excessive drying promotes retro oxa- Michael addition. On the other hand, classical drying at 5 mbar had no effect on the **LGO-*O*-All/LGO** ratio.

Purification of **LGO-*O*-Allyl** by classical silica gel chromatography was not efficient as co-elution was observed between the desired product and both **LGO** and **LGO-Cyrene**. However, a successful one-pot two-step oxa-Michael addition followed by Baeyer-Villiger oxidation has been previously described.[11] Nevertheless, the direct addition of hydrogen peroxide in the presence of a large excess of allyl alcohol was not efficient, probably due to the high dilution of the reaction medium that prevents the oxidation. In consequence, allyl alcohol was distilled off from the crude mixture prior to the addition of H_2O_2. As the presence of a formate intermediate was detected at the end of the reaction (peak at 8.01 ppm in ^{1}H-NMR, Figure S13), an ethanolysis step was added to ensure the complete deprotection of the alcohol. After purification over silica gel, 58% of the desired product was recovered. In our quest to green up further the process (*i.e*, to avoid ethanolysis step), a small amount of water (1 mL.g^{-1} of crude medium) was added during the Baeyer-Villiger oxidation, allowing almost complete hydrolysis without the addition of acid (Figure S13).

To summarize, the retained procedure for the synthesis of HBO-O-All was a one-pot two-step procedure, involving the oxa-Michael addition of allyl alcohol (20 equiv.) into LGO followed by the recovery of the excess of allyl alcohol, then the Baeyer-Villiger oxidation of the crude mixture using H2O2 (0.98 equiv.) and H2O (1 mL/g of crude media).

With **HBO-*O*-All** in hand, assays of enzymatic transesterification with diethyl malonate were attempted (Scheme 2). After a promising first assay using supported lipase B from Candida antarctica (aka, CAL-B or Nov435) in solvent-free condition, a design of experiments (DoE) was conducted on three factors: (i) the temperature (Temp: 70-100 °C), (ii) CAL-B/diethyl malonate ratio (Enz: 320-960 PLU.mmol-1), and (iii) the equivalent of HBO-O-Allyl compared to diethyl malonate (Subs: 2-3 equiv.). Reduced pressure was applied (100 mbar) to ensure the efficient removal of the formed ethanol. A matrix of 15 experiments was generated using Modde 12.0 software and Box-Benkhen design (Table S4). The reaction was performed on 1.5 mmol scale of diethyl malonate and the kinetics of all experiments were monitored by NMR analysis (Figure S14). A reaction time of 5 h was selected to measure two key responses of the DoE: (i) the productivity of the desired dimers, expressed in µmol.min-1, and (ii) the catalytic kinetic constant of the supported enzyme (Pseudo Kcat), expressed in µmol.min-1.genz-1 (Figure 2). These responses allowed to find the suitable conditions for achieving high productivity with the maximum efficiency of the enzyme, thereby minimizing the cost of the reaction.

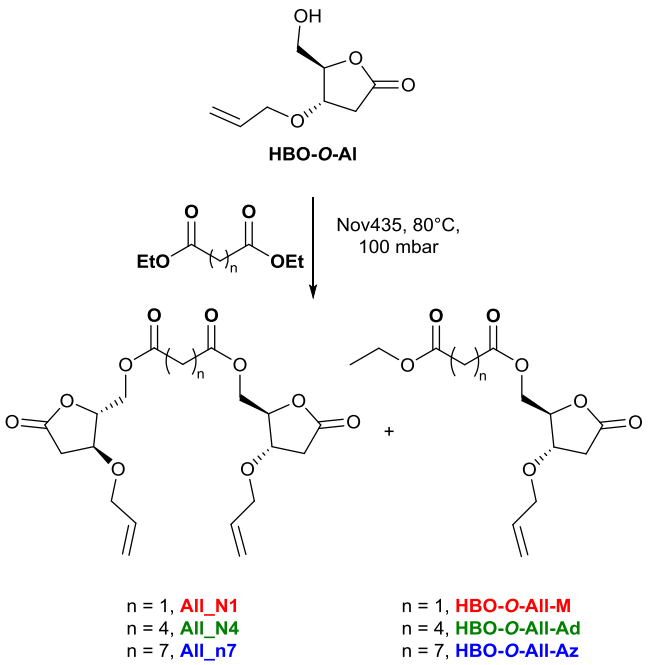

***Scheme 2**. Lipase-mediated condensation of **HBO-O-All** with diethyl esters*

Following the completion of the 15 runs, statistical analysis was performed and revealed good linear regression (R^2 > 0.9) and reproducibility (> 0.90) for both responses. However, the prediction coefficients were deemed acceptable but low (Q^2 < 0.6). To refine the model, two more experiments were carried out at the predicted

points for (i) maximum productivity (81.7 °C, 2.67 equiv, 960 PLU.mmol^{-1}), and (ii) a compromise between maximum productivity and maximum pseudo Kcat (83.1 °C, 2.00 equiv, 352 PLU.mmol^{-1}). Doing so, satisfying summaries of fit were achieved for both responses (Figure S15) through the following equations (Eq. 1 and 2):

$$Productivity = -36.3877 + 0.8859 \times Temp - 0.0057 \times Enz + 5.0749 \times Subs - 0.0040 \times Temp^2 - 0.0989 \times Temp \times Subs + 0.0034 \times Enz \times Subs \quad \text{(Eq. 1)}$$

$$Pseudo\ Kcat = -222.376 + 9.8305 \times Temp - 0.3842 \times Enz + 19.3667 * Subs - 0.0547 * Temp^2 + 0.0021 \times Temp \times Enz - 0.9987 \times Temp \times Subs + 0.0726 \times Enz \times Subs \quad \text{(Eq.2)}$$

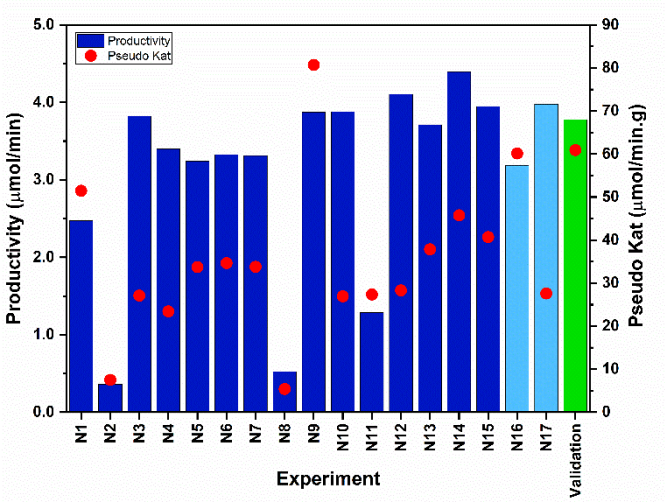

***Figure 2**. Summary of the result of each experiment of the DoE for both productivity and Pseudo Kcat.*

Contour plots of response surfaces revealed that temperature exceeding 90 °C and/or an access of **HBO-*O*-All** have a detrimental effect on the reaction (Figure 3). In addition, it is not possible to achieve both high productivity and Pseudo Kcat under the same conditions. A compromise must be made to ensure good productivity (*i.e.*, reduce time) without using a large amount of enzyme and incurring high cost. The optimal conditions predicted to achieve this compromise are 2 equivalents of **HBO-*O*-All** per unit of diethyl malonate at 82.4 °C in presence of 400 PLU of enzyme per mmol of diethyl malonate. A validation experiment conducted under these conditions confirmed that the recorded productivity and Pseudo Kcat were in accordance with predicted values (Table S4), thus validating the models.

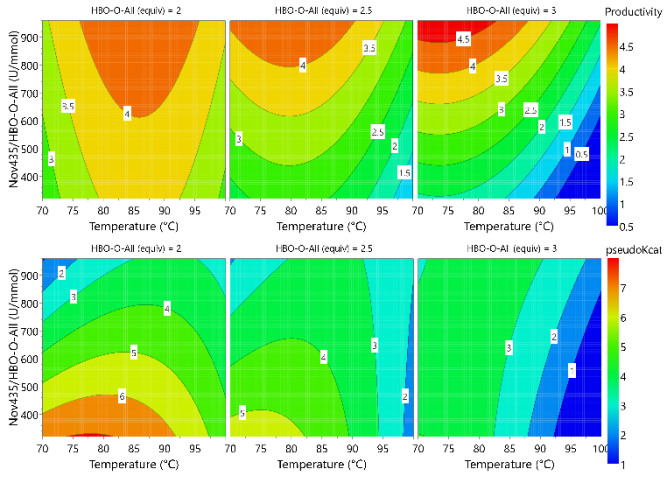

***Figure 3**. Contour plot for productivity (top) and Pseudi Kcat (bottom).*

Once again, the separation of the desired bis-allylated compound, **All_N1**, from **HBO-*O*-All** proved difficult through flash chromatography. However, as **All_N1** is a solid and both the starting material and the mono-allyl malonate are liquids, recrystallization in ethanol was attempted and afforded the desired product (70% yield). The remaining mixture of **HBO-*O*-All** and uncrystallized **All_N1** was reused to further produce **All_N1** (*vide infra*).

In addition, additional experiments were performed using diethyl adipate (n = 4) and diethyl azelate (n = 7) under the optimized conditions to provide longer spacers between the **HBO-*O*-All** moieties (Scheme 2). After 20 h of reaction (Figure 4, Table S5), ^{1}H-NMR was used to compare the results with those of **All_N1**. Remaining **HBO-*O*-All** was

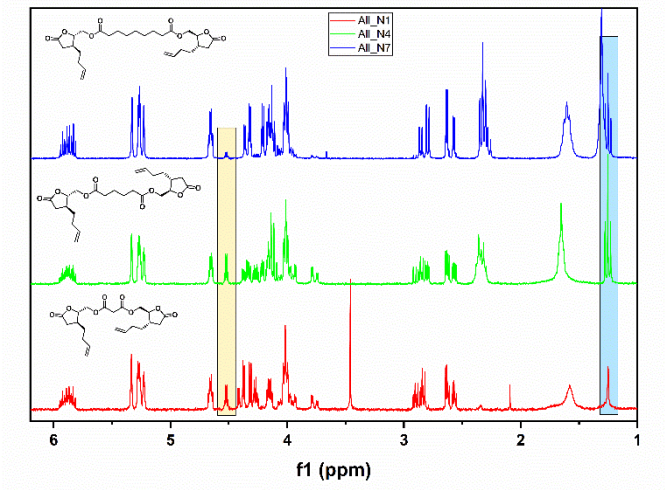

***Figure 4**. ^{1}H-NMR spectra of crude mixture after 20 h of transesterification reaction between **HBO-O-All** and diethyl malonate (red), diethyl adipate (green) and diethyl azelate (blue).*

observed as evidenced by the peak at 4.52 ppm (yellow box in Figure 4). One can notice that when diethyl malonate and diethyl adipate were used, a small amount of **HBO-*O*-All** was still present, however, no remaining **HBO-*O*-All** was detected in the case of diethyl azelate. In addition, the triplet at 1.25 ppm (CH_3 of ethyl moiety, light blue box in Figure 4) showed that the diethyl adipate had a lower reactivity compared to diethyl malonate and diethyl azelate. Indeed, the absence of this triplet in the reaction with diethyl malonate led to think that reaction had stopped due to the lack of diethyl malonate, which probably was partially evaporated from the reaction mixture.

To purify **All_N4** and **All_N7**, flash chromatography over silica gel was used. **All_N7** was recovered in good yield (70%) along with 24% of the mono transesterified compound **HBO-*O*-All-Az**. On the contrary, **All_N4** could not be separated from **HBO-*O*-All** using this technic. To ensure the full conversion of the starting material and thus facilitate the purification, an experiment with a small excess of diethyl adipate (0.6 equiv. instead of 0.5 equiv.) was conducted, allowing to recover pure **All_N4** and **HBO-*O*-All-Ad** in 64% and 26% yield, respectively. It is worth mentioning that the recovered mono-allyl derivatives were used as starting materials for the production of the desired bis-allylated molecules leading to high yields (> 70%).

In order to produce sufficient amounts of monomers for thiol-ene polymerization assays, a scale-up of the monomer synthesis process was performed. First step was started on 20 g (158 mmol) of **LGO**, after Michael addition and subsequent Baeyer-Villiger oxidation, 15.7 g of **HBO-*O*-All** were recovered (63% yield).

Then enzymatic transesterification of diethyl malonate was performed under the optimized conditions, using the concentrated filtrate recovered previously (3.15 g) and 3.0 g of pure **HBO-*O*-All**. After crystallization, 5.0 g of **All_N1** were recovered (65% yield) along with 2.2 g of concentrated filtrate that could be reused for a next batch.

To synthesize **All_N4** and **All_N7**, a small excess of diethyl ester (0.6 equiv) was used to ensure the complete consumption of **HBO-*O*-All**. After flash purification, 5.9 g and 6.5 g (57 and 58% yield) were recovered for **All_N4** and **All_N7**, respectively, along with 4.6 g and 5.3 g of **HBO-*O*-All-Ad** and **HBO-*O*-All-Az**, respectively.

To assess the greenness of this synthetic pathway E-factor[39] and EcoScale[40] were calculated (Table 1).

Green metrics calculation

The E-factor is a measure of the mass of waste generated during the reaction over the mass of desired recovered products, expressed as kgs of waste per kgs of product.[39] In this study, the desired recovered products were both the final bis-allylated compounds and the recovered starting **HBO-*O*-All** and mono-allylated intermediates. EcoScale has been designed to evaluate synthetic pathway at laboratory scale based on 6 criteria: (i) yield, (ii) cost, (iii) safety, (iv) technical set-up, (v) temperature/time and (vi) work-up and purification.[40] Each category provides penalty points that are count down from 100. A score of 100 is attributed to the ideal reaction, above 75 is considered excellent, between 50 and 75 is appropriate, and under 50 is unsuitable. Table 2 shows that all molecules achieved good to excellent EcoScale. The lost points were mainly attributed to reduced yield and flash chromatography purification. In addition, E-factors were very low, in the range of bulk chemicals (Table 2). Note that solvents used for purification (crystallization or flash chromatography) were not counted because they could be recovered in an industrial process.

Table 1. *EcoScale and E-factor for each product of the synthetic pathway.*

Compound	E-Factor	Eco-Sacle
LGO-*O*-All	n.d	79
HBO-*O*-All	1.60	63.5
All_N1	0.04	80
All_N4	0.43	68
All_N7	0.66	71

n.d. not determined

Herein, recyclability of Novozym 435 (*i.e.*, a supported enzyme) was not investigated, however this point could be addressed and, if recyclability is proven, could lead to even lower waste.

UV-Curing Process

The synthetized allyl ethers were investigated as ene monomers in thiol-ene photocurable formulations (Scheme

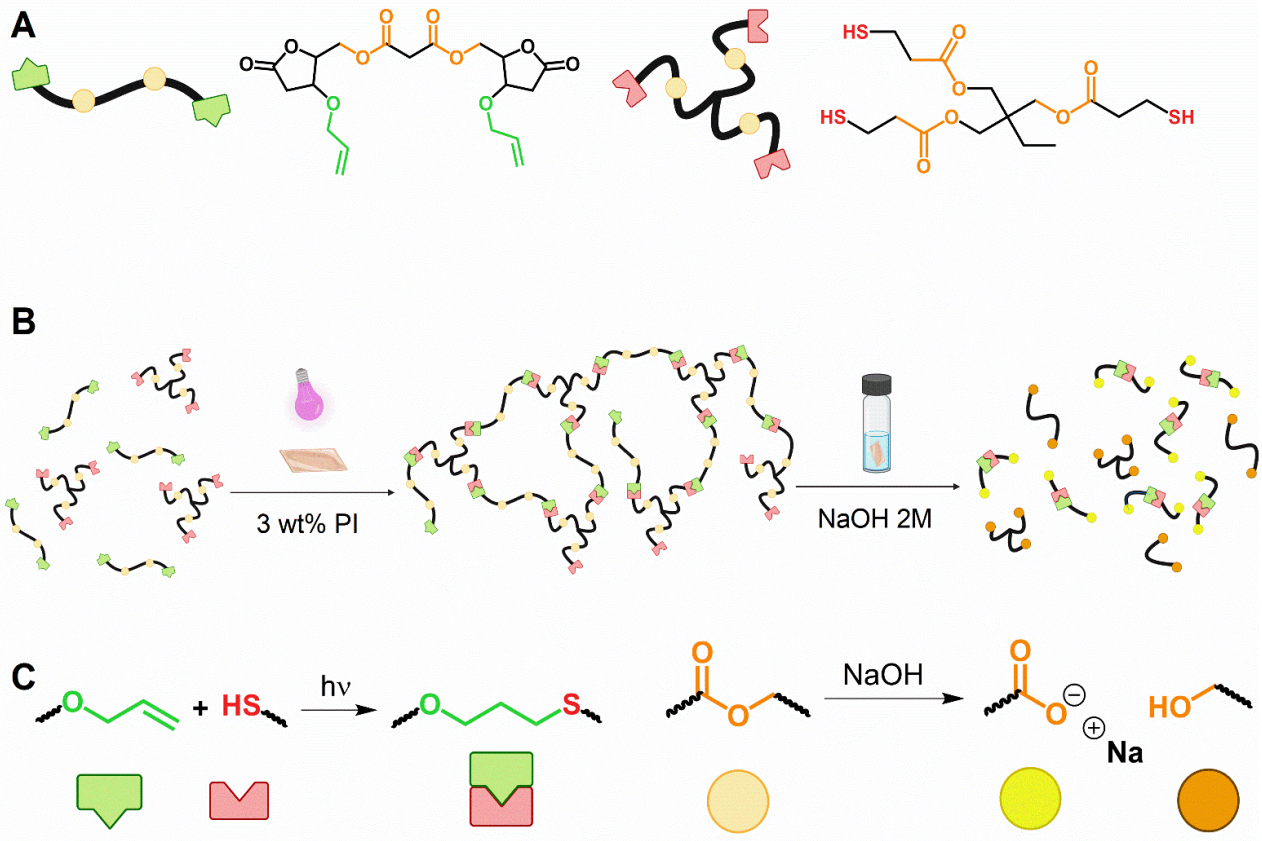

> ***Scheme 3***. *(A)* ***All_N1*** *and* ***TMPMP*** *involved into the UV-curing. (B) curing of the liquid formulation (step 1) and degradation of the cured network (step 2). (C) S-C bond created during the curing and rupture of COO bond during the chemical degradation.*

3). The curing process was investigated by means of real-time FTIR, photo-DSC and photo-rheology.

The polymer network formation was monitored by investigating the disappearance of thiol and ene peaks centered at 2750 cm^{-1} and 1640 cm^{-1}, respectively (Figure S16).

In Figure 5, the conversion curves as a function of the irradiation-time are reported for all the investigated allyl monomers exploited in the photocurable thiol-ene formulation.

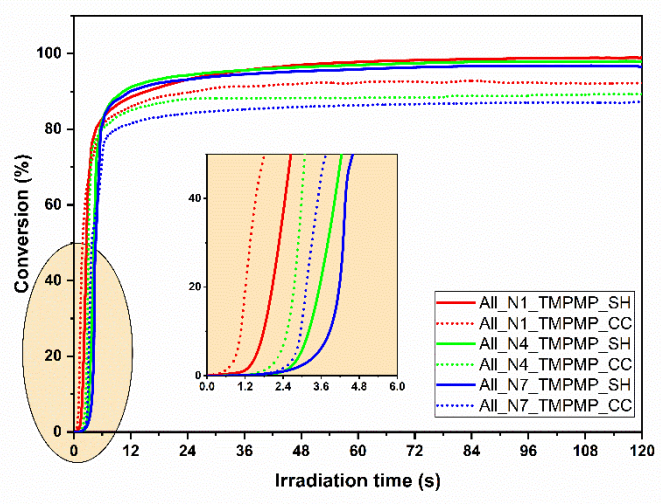

From the real-time FITR, one can conclude that all the formulations tested were extremely reactive showing almost complete conversion. Moreover, the "click" feature, proper of the thiol-ene system, has been confirmed due to the similar conversion trend of S-H and C=C. Finally, a slight difference in the reactivity considering the initial induction time is observed. On another note, the **All_N1_TMPMP** showed the lowest induction time, followed by **All_N4_TMPMP** and then **All_N7_TMPMP**. However, the photocuring reaction for the analysed thin films was found to be complete within approximately 30 seconds for all the investigated formulations.

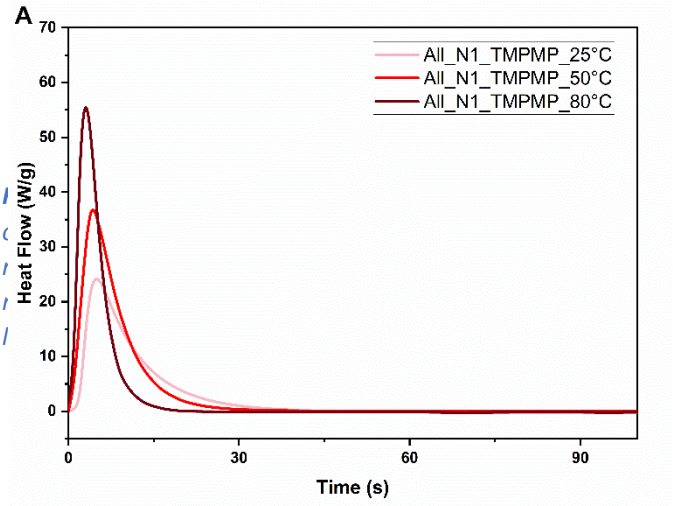

Photo-DSC analysis was carried out on thiol-ene photocurable formulations to confirm the FTIR data. Experiments were performed at different temperature to confirm the effect of this variable on the formulations.

In Figure 6, the thermograms for thiol-ene formulation containing **All_N1** are reported at different temperatures, 80°C, 50°C and 25°C, respectively. The exothermic peak represents the heat of polymerization released during curing process. The height of the peak being related to the rate of polymerization, it is obvious the reaction was faster at 80°C, than at 50°C and 25 °C. The area under the peak represented the total heat of polymerization (Figure S17), the highest value was reached at 80 °C for thiol-ene formulation containing **All_N1** while the other two had the highest value at room temperature.

***Figure 6**. Thermogram for the thiol-ene formulation **All_N1_TMPMP** at different temperatures.*

Figure 7 reports all the enthalpy data plotted against the temperature for the different resins. The influence of the physical state of the ene monomer for **All_N1_TMPMP** affected the conversion at room temperature, limiting final value. All the results for the different formulations investigated are available in supporting information (Table S6).

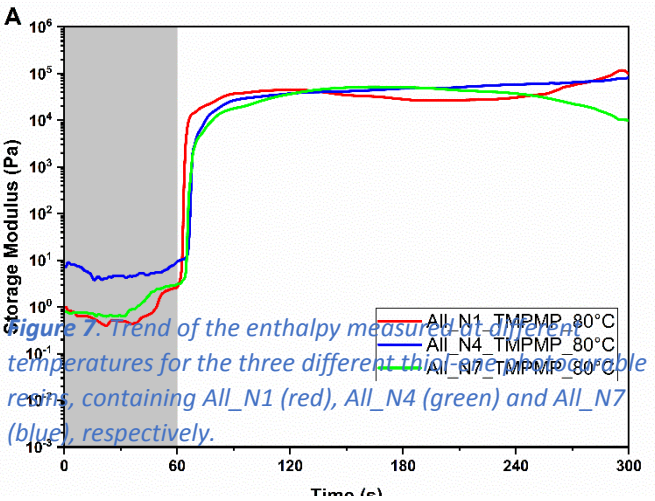

***Figure 7**. Trend of the enthalpy measured at different temperatures for the three different thiol-ene photocurable resins, containing All_N1 (red), All_N4 (green) and All_N7 (blue), respectively.*

Finally, the UV-curing process was further investigated by means of photorheology. In this case, the trend of the storage modulus is followed during the irradiation time.

In Figure 8, the storage modulus curves during irradiation are collected for the three thiol-ene formulations at 80°C. The reaction started as soon as the light reached the sample as shown by the fast increase of the modulus due to the cross-linking reaction that creates rigidity passing from liquid resin to solid thermoset. The photorheology curves showed high reactivity toward the UV-light process, confirming the results obtained by real-time FTIR, indicating that the All_N1 had a lower induction time with respect to the other two formulations. However, as for the previous analysis, all the

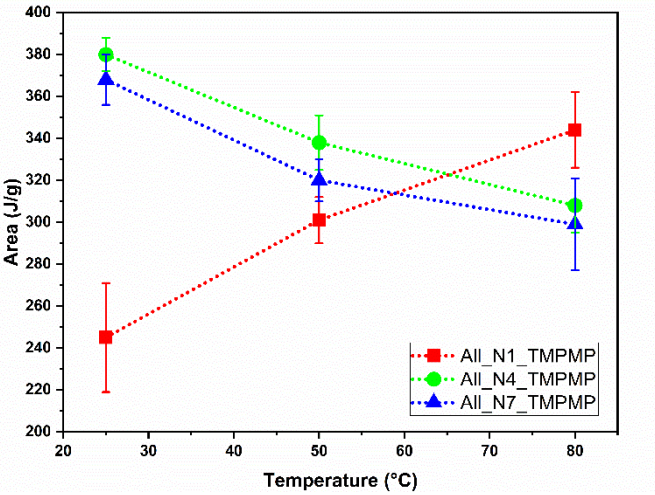

***Figure 8**. Photorheological curves: Storage modulus as a function of the irradiation time at 80 °C for the thiol-ene formulations containing the 3 different allyl-ether resins.*

formulations proved highly reactive as shown by the steep increase of the modulus and the completeness of the reaction in about 60 seconds. Indeed, the plateau of the modulus was reached rapidly indicating a fast crosslinking reaction.

Furthermore, the effect of light-intensity was tested to complete the characterization of the possible variables involved in the UV-process (Figure S18). Data demonstrated that an increase of light intensity reduced the induction time of the reaction, meaning faster reaction due to high dose of irradiation on the sample.

Finally, we have investigated the pot-life stability of the formulation at 80°C. A temperature of 80°C was chosen considering that all the formulations were liquid (**All_N1** returned solid after the mixing stage due to the physical state of the ene monomer) at this temperature. In this case, the rheological isothermal test was done at 80°C and the variation in storage modulus was monitored for about 40 minutes without irradiation. Under such conditions, the storage modulus did not increase over time remaining practically equal to the starting value, demonstrating that the crosslinking is not heat-induced (Figure S19). After 40 minutes, the light was turned on and the variation in storage modulus followed the same trend as the previous test (*i.e.*, UV-irradiation after 60 seconds).

The efficiency of the UV-curing process was also assessed by measuring the gel content on UV-cured samples, which was always above 95% (data collected in Table 2) confirming the success of the crosslinking reaction.

Thermo-mechanical and surface properties characterization of UV-cured network

Once the UV-curing process was investigated, the thermo-mechanical characterization was performed on UV-cured samples. Different analyses were carried out to have a general and complete study of the different properties.

The thermal properties of the thiol-ene networks were investigated by means of DSC analysis (Table 2). The thermosets were compared based on the length of their aliphatic chains, with **All_N1** having the shortest chain, thus leading to the highest T_g (11°C) among the three monomers. The polymer sample made with the ene monomer with four aliphatic carbon atoms had a medium T_g (-1 °C), while the one made with the longest aliphatic chain (seven carbon atoms) had the lowest T_g (-8 °C). The difference of about 20 °C can be attributed only to the chemical structure of the allyl monomer since the ene:thiol ratio functionality was unchanged, and the thiols were the same in all photocurable formulations. This result is in accordance with previous work where the chemical structure of the monomers influenced the final T_g.[46,47]

Viscoelastic properties of the crosslinked networks were investigated by means of DMTA analysis (Figure S20 and Table 2).

Table 2. *Characterization of the UV-Cured networks.*

FORMULATION	T_g [1]	T_g [2]	E' [2]	ν [2]	% gel	Contact angle
	°C	°C	Pa	mmol/dm^3	%	°
All_N1_TMPMP	11.0 ± 0.5	17.5 ± 2.0	2.45 x 10^6	883	98 ± 1	73.5 ± 4.0
All_N4_TMPMP	− 1.0 ± 1.0	1.5 ± 1.5	2.85 x 10^5	108	97 ± 2	78.0 ± 1.5
All_N7_TMPMP	− 8.0 ± 0.5	− 4.0 ± 0.5	9.50 x 10^4	37	96 ± 1	83.0 ± 2.0

[1] DSC analysis, -40 °C to 250 °C, N_2 40 mL/min; [2] DMTA, -20°C to 50°C, air.

The trend of the T_g measured as the maximum of $Tan\delta$ curve is in agreement with the DSC analysis showing the highest T_g value (17.5 °C) for thiol-ene formulation containing **All_N1**. The new information of this analysis was the variation in storage modulus over the temperature. Below the T_g, the three thermosets behave in the same way giving almost the same storage modulus. Then a decrease of E' occurred at the T_g ending at the rubbery plateau. The UV-cured formulation **All_N1_TMPMP** showed the highest value of E' in this region (2.45 x 10^6 Pa),

then the formulation containing **All_N4** showed the medium value and finally the formulation containing **All_N7** had the lowest (9.50 x 10^4 Pa). This translated directly in the crosslinking density of the cured samples, evaluated according to Equation 3 (see ESI) and reported in Table 4. Once again, we can confirm that the chemical structure of the ene monomer influenced the crosslinking density and the rigidity of the network giving an increase in the T_g by reducing the "spacer" length.

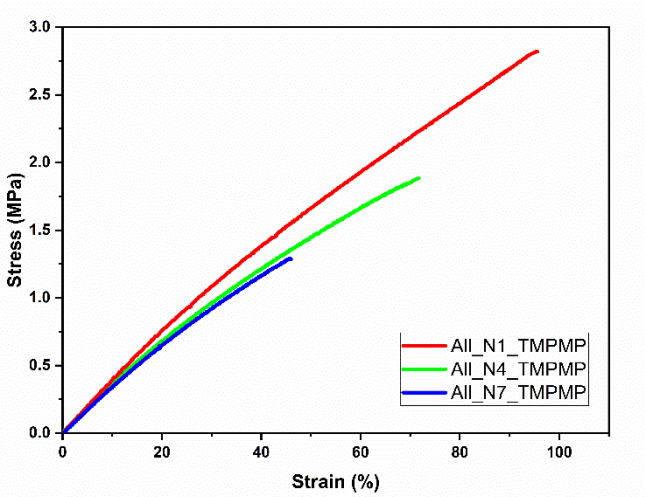

Finally, tensile tests were performed on UV-cured samples. In Figure 9, the characteristic stress-strain curves for the UV-cured thiol-ene network are reported (Table S7 provides all the derived results). The **All_N1_TMPMP** showed the highest Young's modulus due to the high rigidity of the network as well as the highest strength at break (*ca.* 3 MPa). All the three thermosets being tested at room temperature (*i.e.*, above the T_g), the high strain at break was expected. The thiol-ene formulation containing **All_N1** had the best tensile behaviour that could be attributed to the higher rigidity of the UV-cured network, as previously discussed. The longer spacer of the other two allyl-monomers reduced the mechanical performance of the derived thermosets.

***Figure 9**. Stress-strain curves for UV-cured thiol-ene photocurable formulations containing **All_N1** (red), **All_N4** (green) and **All_N7** (blue), respectively.*

Finally, a contact angle measurement on the free surface of cured film was performed. Data showed an increase of the contact angle passing from network containing **All_N1** to **All_N7** that could be explained considering the longer spacer of the allyl monomers. Indeed, the higher hydrophobicity is given by the long aliphatic chain bearing to the allyl ether monomer resulting in a maximum of 83° for **All_N7** (Table S7).

Thermal and chemical degradation

TGA analysis was performed to investigate the thermal stability of the thermoset. The results of the weight loss are reported in Figure 10 with the derivative of the curves. As can be seen from the derivatives, the UV-Cured formulation **All_N1_TMPMP** showed the highest thermal resistance probably due to the high crosslinking density of the achieved polymer network. However, all the three thermosets behave in the same manner with a very similar weight loss. This could be attributed to the identical chemical nature of the mains bond that formed the networks. The main degradation peak around 350 °C can be related to the breaking of the S-C bonds formed during the cross-linking. Then, a second peak, around 450 °C, could be due to the decomposition of the aliphatic chain (*i.e.*, C-C bonds). Indeed, the crosslinked network achieved in the presence of **All_N7** present a higher decrease with respect to the others. The latter could be explained considering the longer spacer thus the higher amount of

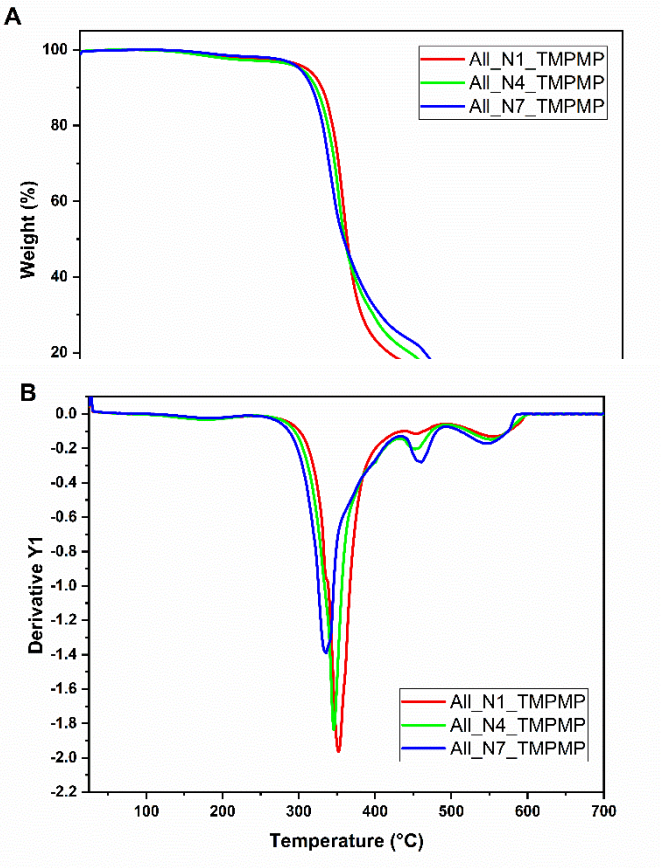

***Figure 10**. (A) Weight loss development over temperature for **All_N1_TMPMP** (red), **All_N4_TMPMP** (green) and **All_N7_TMPMP** (blue). (B) Derivatives obtained from TGA curve.*

aliphatic part in the network. The last peak around 550 °C represents the final degradation of the network giving almost no residual char. The slightly differences seen in the derivative are highlighted in Table S8.

A chemical degradation study of the cured samples was carried out in an alkaline environment to investigate the stability of the ester bonds present into the network. The results depicted in Figure 11 show the mass lost over time. The **All_N1_TMPMP** showed the faster degradation process, followed by **All_N4_TMPMP** and **All_N7_TMPMP**. The observed higher resistance to degradation (i.e., lower weight loss over time) is directly linked to the chain length of the diester moiety of the diallyl monomer. We then assume that the increase of the chain length results in a higher hydrophobicity and thus a slower hydrolysis, accounting for the different degradation kinetics observed.

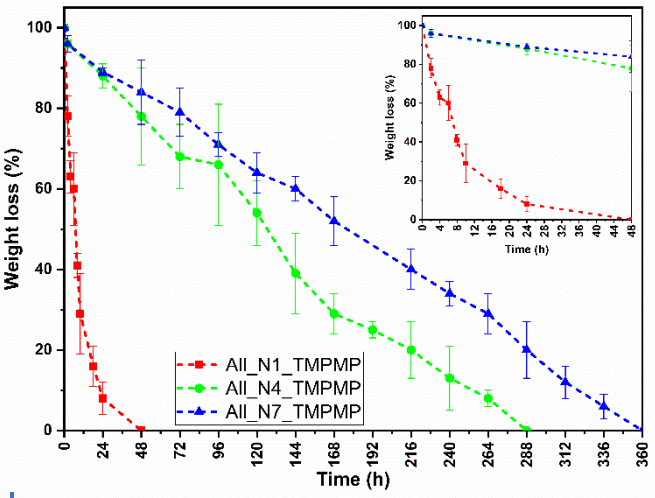

***Figure 11**. Degradation study for the three thiol-ene system, **All_N1_TMPMP** (red), **All_N4_TMPMP** (green) and **All_N7_TMPMP** (blue).*

3D-printing

The designed thiol-ene photocurable formulations were also tested in DLP 3D printing. Firstly, the photo-rheology proved the high reactivity and the low induction time even at low light intensity (ESI, Figure S16). These two features are crucial to have reaction time comparable with the printing time and to be able to create self-stain structure by 3D printing. The complete reaction was reached in less than 30 seconds proving the possibility to employ DLP. Another key feature of the resins is the viscosity (Figure S 21). Controlling this parameter is essential if one wants to cover properly the VAT and to form an uniform layer. The three resins showed good viscosity at 80 °C, however the **All_N1_TMPMP** required constant heating to stay liquid for prolonged time (*i.e.*, time of printing). Thus, the other resins, **All_N4_TMPMP** and **All_N7_TMPMP** were selected, tested and used for the 3D printing at room temperature. The viscosity remained suitable at 25 °C (Figure S21B). The printing parameters for each formulation (*i.e.*, light intensity, exposure time, and burn-in layers) were empirically set considering the information obtained by photo-rheology and real-time FITR analysis while velocity of the platform movement was set considering viscosity of the formulations.

The thiol-ene formulations containing **All_N4** and **All_N7** were printed with interesting result in terms of reproducibility. A honeycomb structure was produced for both resins. A focus on the use of **All_N7_TMPMP** was performed producing a further structure. Figure 16 shows the photograph of the printed objects and the analysis performed with a 3D scanner. Note that one can analyze the dimensional differences between the CAD file used for the realization of the shape and the 3D-printed object. Figure 12 gives an idea of the boundaries in which the printing has been done. The precision of the printing process can be defined by the shape fidelity of the printed object to the reference CAD file. A comparison between the digital file and the printed object was done to prove the accuracy. This test creates a three-dimensional model of the object that can then be compared via software to the starting design, creating an overlay map that displays the deviation. The mean value remained in a very tight range with a 0.42% with respect to the CAD file; the green zone, representing the most accurate area was identified with a range between -100 to +100 nm with respect to the original file (Figure 12 D).

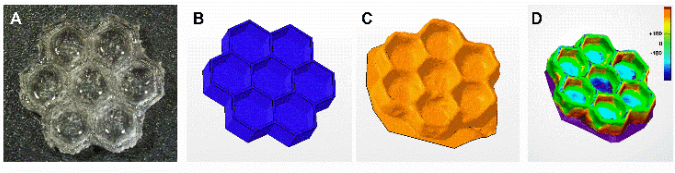

***Figure 12.** (A) Picture of the 3D-printed object by **All_N7_TMPMP**; (B) CAD file of honeycomb with dimensions of 11.27 x 11.66 x 2.12 mm (x, y and z axis, respectively); (C) scanner detection of the 3D-printed shape inserted in the 3D scanner with magnesium stearate powder; (D) comparative analysis of 3D-printed object and CAD file.*

The discordance, irregularities and divergences can be attributed to several factors, from machine errors to resin limitations. The process-dependent errors could be printer resolution, printing errors, scanner precision and difficulty to properly detect areas of the structure. In addition, the non-uniform distribution of magnesium stearate powder on the surface of the object, which is used to improve scanning efficiency, as well as the presence of a support to enable the correct acquisition of the images, could create artefacts. Furthermore, the reactivity of the formulation can be a cause of limitation of the accuracy as well as the lack of a complete and proper printing formulation with a color dye or radical inhibitor. The dye could limit the polymerization and increase the absorbance of the light in the desiderate region to increase the efficiency. This could be a future prospective to maximize and optimize the efficiency of the 3D-printing. Additional shapes printed with **All_N4_TMPMP** and **All_N7_TMPMP** can be found in Figure S22 and S23, respectively.

Conclusion

In this study, we demonstrated the efficiency of the chemo-enzymatic synthesis of tunable bis-allyl derivatives from **LGO**. This pathway is easily scalable and has achieved high EcoScale and very low E-factor.

UV-curing of the aforementioned monomers was used to create a degradable thiol-ene network whose final properties were influenced by the chemical structure of the ene monomer used in the crosslinking reaction. Among the synthesized monomers, **All_N1_TMPMP** exhibited the best performance in term of thermo-mechanical behaviour due to the shortest aliphatic spacer between the ester bonds, therefore leading to a higher crosslinking density. We also investigated the potential recyclability of the cross-linked network by exposition to alkaline environment, revealing the possibility of an end-of-use for these materials. The **ALL_N1_TMPMP** UV-cured samples showed also the faster and complete chemical degradation in alkaline conditions. Furthermore, we explored the feasibility of the thiol-ene formulation in a 3D-printing domain and successfully printed complex objects with **All_N4_TMPMP** and **All_N7_TMPMP**.

Overall, this study demonstrates the possibility to use renewable resources, such as **LGO**, to develop new bio-based resin for thiol-ene chemistry, opening the possibility for DLP 3D-printing in various applications. Future prospects include an in-depth study of the degradability of these materials to assess the possibility of reusing the degradation products, and explore the potential of **LGO** as a bio-based platform to produce high-performance 3D-printed green materials.

Author Contributions

SF, FA and MS **conceptualized** this work. SF **supervised** the monomer syntheses. ALF and LP developed **methodology** and **wrote the original draft**. ALF, LP, SB and AD performed **investigation**. SF, FA, MS **reviewed** the draft. FA and MS gave access to all needed **resources**. All authors have given approval to the final version of the manuscript. ‡These authors contributed equally.

Conflicts of interest

There are no conflicts to declare.

Acknowledgements

URD ABI acknowledges the Grand Reims, Grand Est Region and Conseil Départemental de la Marne for their financial support.

References

1 R. Geyer, J. R. Jambeck and K. L. Law, Sci Adv, 2017, 3, 1–5.
2 J. J. Bozell and G. R. Petersen, Green Chemistry, 2010, 12, 539–554.
3 G. John, S. Nagarajan, P. K. Vemula, J. R. Silverman and C. K. S. Pillai, Prog Polym Sci, 2019, 92, 158–209.
4 L. Pezzana, E. Malmström, M. Johansson and M. Sangermano, Polymers (Basel), 2021, 13, 1530.
5 R. Auvergne, S. Caillol, G. David, B. Boutevin and J.-P. Pascault, Chem Rev, 2014, 114, 1082–1115.
6 L. Pezzana, G. Melilli, N. Guigo, N. Sbirrazzuoli and M. Sangermano, React Funct Polym, 2023, 185, 105540.
7 Circa group, FuracellTM process, https://circa-group.com/technology/, (accessed 21 March 2023).
8 J. E. Camp and B. W. Greatrex, Front Chem, 2022, 10, 1–9.
9 F. Diot-Néant, E. Rastoder, S. A. Miller and F. Allais, ACS Sustain Chem Eng, 2018, 6, 17284–17293.
10 S. Fadlallah, A. A. M. Peru, L. Longé and F. Allais, Polym Chem, 2020, 11, 7471–7475.
11 F. Diot-Néant, L. M. M. Mouterde, C. Veith, J. Couvreur, S. A. Miller and F. Allais, ACS Sustain Chem Eng, 2022, 10, 10132–10143.
12 S. Fadlallah, Q. Carboué, L. M. M. Mouterde, A. Kayishaer, Y. Werghi, A. A. M. Peru, M. Lopez and F. Allais, Polymers (Basel), 2022, 14, 1–13.

13 S. Fadlallah, A. Kayishaer, M. Annatelli, L. M. M. Mouterde, A. A. M. Peru, F. Aricò and F. Allais, Green Chemistry, 2022, 24, 2871–2881.
14 S. Fadlallah, L. M. M. Mouterde, G. Garnier, K. Saito and F. Allais, 2020, pp. 77–97.
15 Y. Yagci, S. Jockusch and N. J. Turro, Macromolecules, 2010, 43, 6245–6260.
16 C. E. Hoyle, C. N. Bowman, C. N. Bowman and C. E. Hoyle, Angewandte Chemie international edition, 2010, 49, 1540–1573.
17 N. B. Cramer and C. N. Bowman, Polym Chem, 2001, 39, 3311–3319.
18 M. Atilla Tasdelen and Y. Yagci, Angewandte Chemie International Edition, 2013, 52, 5930–5938.
19 M. K. Porwal, M. M. Hausladen, C. J. Ellison and T. M. Reineke, Green Chemistry, 2023, 25, 1488–1502.
20 M. Claudino, J.-M. Mathevet, M. Jonsson and M. Johansson, Polym Chem, 2014, 5, 3245–3260.
21 A. Stamm, M. Tengdelius, B. Schmidt, J. Engström, P. O. Syrén, L. Fogelström and E. Malmström, Green Chemistry, 2019, 21, 2720–2731.
22 D. B. Larsen, R. Sønderbæk-Jørgensen, J. Duus and A. E. Daugaard, Eur Polym J, 2018, 102, 1–8.
23 L. Pezzana, G. Melilli, P. Delliere, D. Moraru, N. Guigo, N. Sbirrazzuoli and M. Sangermano, Prog Org Coat, 2022, 173, 107203.
24 T. Modjinou, D.-L. Versace, S. Abbad-Andallousi, N. Bousserrhine, J. Babinot, V. V. Langlois and E. Renard, ACS Sustain Chem Eng, 2015, 3, 1094–1100.
25 H. Seker and E. Çakmakçi, Journal of polymer Science, 2020, 58, 1105–1114.
26 L. Pezzana and M. Sangermano, Prog Org Coat, 2021, 157, 106295.
27 S. C. Ligon, R. Liska, J. Rgen Stampfl, M. Gurr, R. Mü and ‖ H B Fuller, Chem Rev, 2017, 117, 10212–10290.
28 M. Shahbazi and H. Jä, Cite This: ACS Appl. Bio Mater, 2020, 2021, 369.
29 A. Bagheri and J. Jin, ACS Appl Polym Mater, 2019, 1, 593–611.
30 H. Quan, T. Zhang, H. Xu, S. Luo, J. Nie and X. Zhu, Bioact Mater, 2020, 5, 110–115.
31 E. Sanchez-Rexach, T. G. Johnston, C. Jehanno, H. Sardon and A. Nelson, Chemistry of Materials, 2020, 32, 7105–7119.
32 V. S. D. Voet, J. Guit, K. Loos, V. S. D. Voet, J. Guit and K. Loos, Macromol Rapid Commun, 2020, 42, 1–11.
33 A. Navaruckiene, S. Kasetaite and J. Ostrauskaite, Rapid Prototyp J, 2019, 26, 402–408.
34 A. Navaruckiene, D. Bridziuviene, V. Raudoniene, E. Rainosalo, J. Ostrauskaite and R. Palmese, Materials, 2021, 14, 1–20.
35 D. Merckle, E. Constant and A. C. Weems, ACS Sustainable Chemistry and Engineering, 2021, 9, 12213–12222.
36 E. Constant, O. King and A. C. Weems, Biomacromolecules, 2022, 23, 2342–2352.
37 G. Bonneau, A. A. M. Peru, A. L. Flourat and F. Allais, Green Chemistry, 2018, 20, 2455–2458.
38 F. Allais, G. Bonneau, A.A.M. Peru, A.L. Flourat Method for converting Levoglucosenone into 4-Hydroxymethyl butyrolactone or 4-Hydroxymethyl butenolide without using any organic solvent and catalyst WO 2018/007764 A1, 2018.
39 R. A. Sheldon, Green Chemistry, 2007, 9, 1273–1283.
40 K. Van Aken, L. Strekowski and L. Patiny, Beilstein Journal of Organic Chemistry, 2006, 2, 1–7.
41 M. Janvier, L. Hollande, A. S. Jaufurally, M. Pernes, R. Ménard, M. Grimaldi, J. Beaugrand, P. Balaguer, P. H. Ducrot and F. Allais, ChemSusChem, 2017, 10, 738–746.
42 F. Diot-néant, L. M. M. Mouterde, J. Couvreur, F. Brunois, S. A. Miller and F. Allais, Eur Polym J, 2021, 159, 1–8.
43 Kawai, M. Isobe and S. C. Peters, Aust J Chem, 1995, 48, 115–131.
44 B. T. Sharipov, A. A. Pershin and F. A. Valeev, Mendeleev Communications, 2017, 27, 119–121.
45 S. Fadlallah, Q. Carboué, L. M. M. Mouterde, A. Kayishaer, Y. Werghi, A. A. M. Peru, M. Lopez and F. Allais, Polymers (Basel), 2022, 14, 1–13.
46 L. Pezzana, M. Mousa, E. Malmström, M. Johansson and M. Sangermano, Prog Org Coat, 2021, 150, 105986.
47 L. Pezzana, G. Melilli, P. Delliere, D. Moraru, N. Guigo, N. Sbirrazzuoli and M. Sangermano, Prog Org Coat, 2022, 173, 107203.